# DIRECT NUMERICAL SIMULATION OF MOMENTUM AND HEAT TRANSPORT IN IDEALIZED CZOCHRALSKI CRYSTAL GROWTH CONFIGURATIONS

**Claus Wagner**
Institute for Aerodynamics and Flow Technology,
German Aerospace Center
Bunsenstr. 10, 37073 Göttingen, Germany
claus.wagner@dlr.de

**Rainer Friedrich**
Fachgebiet Strömungsmechanik,
Munich University of Technology
85748 Garching, Germany
r.friedrich@lrz.tu-muenchen.de

## ABSTRACT

Turbulent momentum and heat transport in idealized Czochralski crystal growth configurations is investigated by means of direct numerical simulation. The analysis of the flow data focuses on the influence of crystal and crucible rotation on the flow structures and the development of temperature fluctuations. A numerical parameter study is performed to investigate how the variation of the numerous flow parameters affect the turbulent transport processes. Finally, a direct numerical simulation is conducted with parameters taken from experiment in order to allow a direct comparison between numerical and experimental results.

It is found that the counter-rotation of the crystal and crucible leads to a complex flow, which is characterized by three major recirculation zones, if crucible rotation dominates the flow. The dynamics of the flow are controlled by centrifugal forces counteracting buoyancy and surface tension effects. High temperature fluctuations are created within or close to the crystallization zone. Neither a variation of the melt height, nor a reduction of the crystal rotation rate or a change of the Grashof and Marangoni numbers has a major effect on the bulk flow structure and overall heat transfer. Increasing rotation of the crystal changes the bulk flow structure strongly and leads to an increased value of maximum rms temperature fluctuations, the position of which is shifted towards the crucible bottom. A shifted position of maximum rms temperature fluctuations is also observed if heat radiation across the free surface is taken into account.

## INTRODUCTION

Semiconductor industry has a high demand on pure silicon crystals, which are needed to produce all sorts of electronical devices. Around 90% of the worldwide silicon demand is grown utilizing the Czochralski process. In Czochralski crystal growth configurations the low Prandtl number silicon melt is kept in a cylindrical crucible. Heating the crucible side wall gives rise to buoyant convection. The crystal is pulled from the free surface at rates between a few millimeters to centimeters per second. Along the free surface, Marangoni convection develops due to radial temperature gradients between the side wall and the comparably cold cylindrical crystal. Crucible and crystal are commonly rotated in opposite directions, so that centrifugal forces counteract buoyancy and surface-tension driven convection. In addition, thermal conduction and heat radiation at the free surface induce losses of heat to the surrounding.

The fluid flow and heat transfer processes in the melt of a Czochralski growth system are extremely complex, since several effects arise simultaneously in this process. The associated instabilities are the Rayleigh-Benard, baroclinic and Küppers-Lortz instability. They lead to time-dependent three-dimensional motions in the melt, which influence the transport of dopant, impurities and heat to the crystal/melt interface and thus determine the purity of the crystal.

That the Czochralski melt flow is turbulent, has been suspected about thirty years ago by Wilcox and Fulmer (Wilcox 1965) who used thermocouples to measure temperature fluctuations in a calcium fluoride melt ($Pr = O(1)$) confined in a rather small crucible ($Gr = 10^6$). Most of the experimental investigations alluding to the fluctuating nature of the flow have been done in rather small melt volumes of high Prandtl number. One reason might be that the experimental investigation of these low Prandtl number turbulent flow and heat transport processes faces lots of difficulties. In large scale growth systems the flow is mostly turbulent, the melts are usually opaque and due to their high freezing temperature unsuitable for most tracer particles.

The convection of a transparent fluid (Prandtl number O(1)) forced by rotation of the crystal in a non-rotating heated crucible was investigated in the experiment of Jones (Jones 1989). In the vicinity of the crystal he observed temperature fluctuations of high amplitude. From temperature measurements by Kuroda et al. (Kuroda 1982) it is known that temperature fluctuations of large amplitude are responsible for an increased concentration of micro-defects in the crystal.

Vizman et al. (Vizman 2001) recently reported temperature measurements at different locations within a silicon melt kept in a small industrial Czochralski crucible of radius $R_c = 0.17m$. For the same configuration Enger et al. (Enger 2001) performed underresolved numerical simulations on structured but curvilinear grids for Grashof numbers up to $Gr = 10^9$. They showed that their simulated temperature data agree favorably with the temperature measurements of Vizman et al. (Vizman 2001).

It is the aim of this work to investigate the influence that varying rotation rates of crucible and crystal, heat radiation at the free surface, different melt heights and crucible dimensions have on the development of temperature fluctuations at high Grashof numbers ranging from $1.0 \cdot 10^8$ to $2.0 \cdot 10^9$. This is done by means of Direct Numerical Simulation on cylindrical grids with up to 4.5 million grid points. In this study the Czochralski configuration is idealized in the sense that a flat free surface and a flat crystal/melt interface are assumed.

## NUMERICAL METHOD

The incompressible Navier-Stokes equations in Boussinesq ap-

proximation

$$\nabla \cdot \vec{u} = 0 \tag{1}$$

$$\partial \vec{u}/\partial t + \nabla \cdot (\vec{u}\vec{u}) = -\nabla p + \nabla^2 \vec{u}/Gr + \vec{b} \tag{2}$$

$$\partial T/\partial t = -(\vec{u} \cdot \nabla)T + \nabla^2 T/(Pr\sqrt{Gr}) \tag{3}$$

are integrated applying Schumann's volume balance procedure (Schumann 1973) in cylindrical coordinates. The nabla operator $\nabla$ and the velocity vector $\vec{u} = (u_z, u_\varphi, u_r)$ in equations (1) - (3) are non-dimensionalized with the crucible radius $R_c$ and the buoyancy velocity scale $(\alpha g R_c(T_c - T_s))^{1/2}$. A dimensionless temperature is defined by $(2T - (T_c + T_s))/(2(T_c - T_s))$. $\vec{b}$ represents the dimensionless buoyancy vector, $p$ the dimensionless pressure and $t$ the dimensionless time.

The Grashof number $Gr = (\alpha g R_c^3(T_c - T_s))/\nu^2$ and the Prandtl number $Pr = \nu/\gamma = 0.0175$ contain the thermal expansion coefficient $\alpha = 10^{-4} 1/K$, the kinematic viscosity $\nu = 3.12 \cdot 10^{-7} m^2/s$, the thermal conductivity $\gamma$ and the gravitational acceleration $g$. Their values are those of a Si-melt.

Integrating equations (1) - (3) following Schumann (Schumann 1973) provides a set of spatially discrete equations on staggered grids. Utilizing second order central interpolation and differentiation schemes leads to a method which is suitable for DNS. Within a second order semi-implicit time integration scheme all convection/diffusion terms of the momentum equations containing derivatives in circumferential direction as well as all diffusive terms of the heat conduction equation are integrated implicitly by a Crank-Nicholson time step. The remaining convection terms are treated explicitly with a Leapfrog time step, which is restricted by a linear stability criterion.

A fractional step approach provides the oscillation-free coupling between pressure and velocity fields and leads to a three dimensional Poisson equation for the pressure correction, which has to be solved at each time step. A 3D-Helmholtz equation has to be solved due to the implicit treatment of the temperature. The direct solutions of these elliptic problems are obtained using FFT's in $\varphi$-direction and cyclic reduction algorithms for the remaining 2D Helmholtz problems. The 1D Helmholtz problems associated with the implicit treatment of the $\varphi$-derivatives in the momentum equations are solved by a tridiagonal matrix algorithm.

## BOUNDARY CONDITIONS & GEOMETRICAL OUTLINE

The outline of the cylindrical domain of computation is presented in Fig. 1. A cylindrical crystal of radius $R_s$ the axis of which coincides with the axis of the cylindrical crucible grows out of a melt of height $H$ at the free surface. The freezing temperature of silicone (1485 K) defines the dimensionless crystal temperature $T_s = -0.5$. Heating at the crucible sidewall is modeled by constant temperature $T_c = 0.5$.

Boundary conditions at the side and bottom walls of the crucible and the interface to the crystal are the impermeability condition for the wall normal components and the no slip conditions for the tangential velocity components. The solid-body rotation of the crucible and the crystal is imposed on the circumferential velocity component at the crystal/melt and crucible-bottom/melt boundaries. Fixed temperature boundary conditions are specified at the side wall of the crucible and the crystal/melt interface. For most cases the bottom of the crucible and the free surface is assumed to be adiabatic. The flat free surface further forces the axial velocity component to vanish. Finally, at the free surface, strain and heat radiation boundary conditions (4) - (6) are discretized.

$$\partial u_r/\partial z = -Ma/(Pr\sqrt{Gr})\partial T/\partial z \tag{4}$$

$$\partial u_\varphi/\partial z = -Ma/(Pr\sqrt{Gr})\partial T/(r\partial\varphi) \tag{5}$$

$$\partial T/\partial z = -(4R_c\varepsilon\sigma T_s^3/\lambda)T - \varepsilon\sigma R_c(T_s^4 - T_h^4)/(\lambda\Delta T) \tag{6}$$

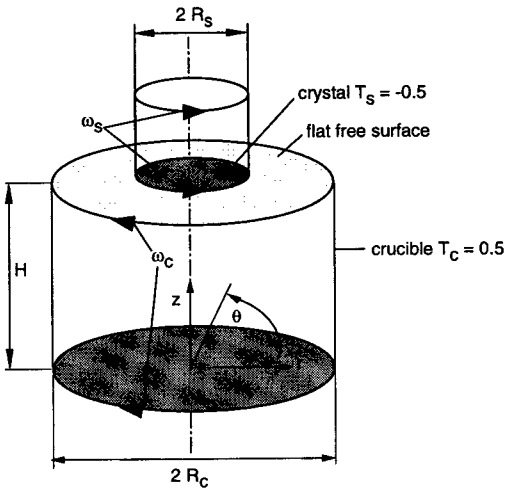


Figure 1: Geometry of the Czochralski configuration.

where $Ma = (cR_c(T_c - T_s))/\gamma$ defines the Marangoni number which contains the capillary coefficient $c = 0.149$ according the value for a Si-melt open to the ambient air. Furthermore, $\sigma = 5.75 \cdot 10^{-8} J/(sm^2K^4)$ denotes the radiation constant, $\varepsilon = 0.23$ the emission coefficient, $\lambda = 46.6 J/(smK)$ the thermal conductivity and $T_h$ the background temperature.

## RESULTS

The different flow parameters used in the direct numerical simulations (DNS) discussed below are summarized in Table 1. The parameter combination of $DNS_1$ defines the reference case of a crucible with the radius $R_c = 4.8cm$ rotating at 16.8 rpm and having a temperature difference $\Delta T = T_c - T_s = 91.4K$. This leads to a Grashof number $Gr = 10^8$, a Marangoni number $Ma = 36000$ and a Reynolds number based on the angular frequency $\omega_s$ and the radius of the crystal of $Re = \omega_s R_s^2/\nu = 4712$. Furthermore, a rotation ratio $\omega_c/\omega_s = -0.7$ was specified. For all simulations grids with $N_\varphi = 128$ points in $\varphi$-direction were used. Regarding the axial and radial directions the number of grid points $N_z$ and $N_r$ used are summarized in Table 1. With $DNS_2$ - $DNS_7$ we study the influence of parameter variations on the turbulent momentum and heat transport comparing the results to those obtained in $DNS_1$. For $DNS_1 - DNS_7$ the ratio between the crystal and crucible radius was fixed to $R_s/R_c = 0.5$. Solely for $DNS_8$, which was performed to compare our results to temperature measurements by Wacker Siltronic (Wacker 2001), a ratio $R_s/R_c = 0.294$ was specified.

Table 1: Flow parameters and grid points of turbulent Czochralski flow simulations ($N_\varphi = 128$ in all cases).

| DNS | 1 | 2 | 3 | 4 |
|---|---|---|---|---|
| $N_z, N_r$ | 196,174 | 66,92 | 66,92 | 130,130 |
| $Gr$ | $10^8$ | $10^8$ | $10^8$ | $10^8$ |
| $Ma$ | 36000 | 36000 | 36000 | 36000 |
| $Re$ | 4712 | 4712 | 76.7 | 20950 |
| $\omega_c/\omega_s$ | −0.7 | −0.7 | −43.0 | −0.1 |
| $H/R_c$ | 1.0 | 0.5 | 1.0 | 1.0 |
| DNS | 5 | 6 | 7 | 8 |
| $N_z, N_r$ | 196,196 | 130,130 | 130,130 | 131,174 |
| $Gr$ | $10^9$ | $10^8$ | $10^8$ | $1.6 \cdot 10^9$ |
| $Ma$ | 70000 | 36000 | 5000 | 28000 |
| $Re$ | 14902 | 4712 | 4712 | 16782 |
| $\omega_c/\omega_s$ | −0.7 | −0.7 | −0.7 | −0.25 |
| $H/R_c$ | 1.0 | 1.0 | 1.0 | 0.5 |

$DNS_1$ was started at $t = 0$ with the initial field

$$u_r = u_\varphi = u_z = 0, \quad T = T_c + T_{random} \tag{7}$$

where $T_{random}$ stands for numerically created random temperature perturbations between $-0.1$ and $0.1$. After the solution of $DNS_1$ reached a statistically steady state, an instantaneous flow field was interpolated on the other grids to define the initial turbulent fields for $DNS_2$ - $DNS_8$. After each of the simulations reached a statistically steady state more than 1500 realizations with a time lag of 50 time steps were averaged in circumferential direction and in time to obtain stable statistical values.

### Instantaneous fields

In a perspective view contours of the radial velocity component and of the temperature field which were calculated in $DNS_1$ are shown in Fig. 2. Buoyancy drives the melt upwards along the heated crucible side wall as indicated by the wall parallel isotherms in this region (Fig. 2 bottom). The flow turns inward at the meniscus and moves along the free surface creating a flow towards the cylinder axis. In the vicinity of the crystal the fluid encounters the outward flow driven by centrifugal effects due to crystal rotation. These two counteracting mechanisms lead to local ejections of cold fluid into the buoyancy driven hot recirculation zone creating large amplitude temperature fluctuations there, as indicated by the dashed lines at the free surface in Fig. 2 bottom.

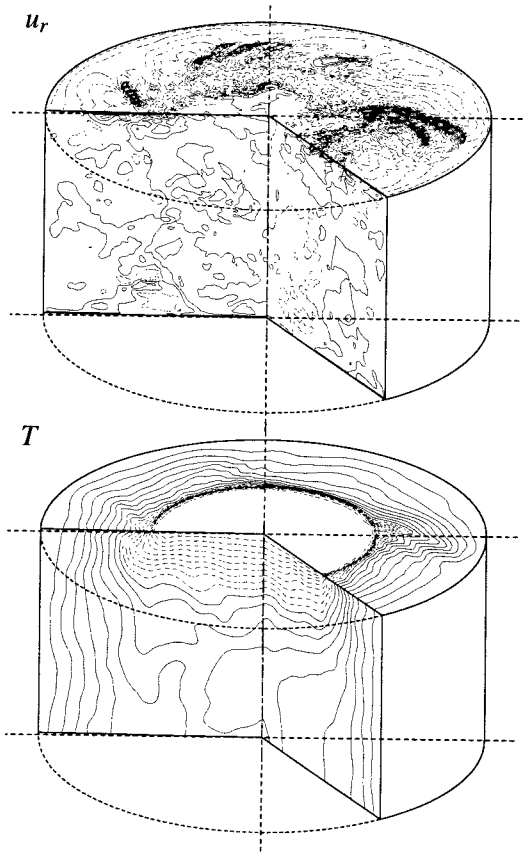


Figure 2: Snapshot of the instantaneous radial velocity component $u_r$ ($(u_r)_{max} = 1.497$, $(u_r)_{min} = -1.581$) and the instantaneous temperature $T$. Solid/dashed contour lines represent positive/negative values.

### Statistically averaged flow fields

Streamlines of the mean velocities in a $(z,r)$-plane in Fig. 3 reveal three major recirculation zones for $DNS_2$. One of these cells develops underneath the crystal, the other one along the crucible wall and the third one just underneath the free surface.

Similar to the instantaneous temperature field the isotherms of the mean temperature are vertically orientated near the side wall of the crucible as depicted in Fig. 4. The cold fluid underneath the crystal is driven outward by the crystal rotation creating high temperature gradients when heated up by the fluid of the buoyancy driven recirculation zone. The mean isotherms underneath the crystal are aligned with the crystal/melt interface fulfilling a necessary condition for a vertically uniform crystal growth. Also benefitial for solidification is the encapsulation of cold fluid underneath the crystal since this prevents undercooling of the melt.

Contours of rms temperature fluctuations are presented in Fig. 5 The position of the maximum rms temperature fluctuation is located within the crystallization zone close to the crystal edge with values of $T_{rms} = 0.17(\approx 15.4K)$. Instantaneous temperature fluctuations even reach values of $28K$. These large temperature fluctuations are the most probable cause of micro-defects in the crystal.

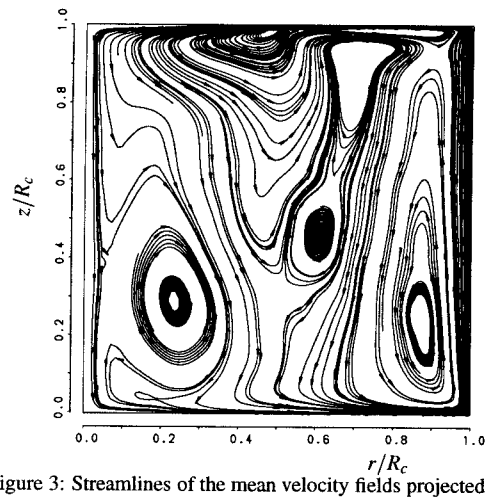


Figure 3: Streamlines of the mean velocity fields projected into $(z,r)$-planes of $DNS_1$ (reference case).

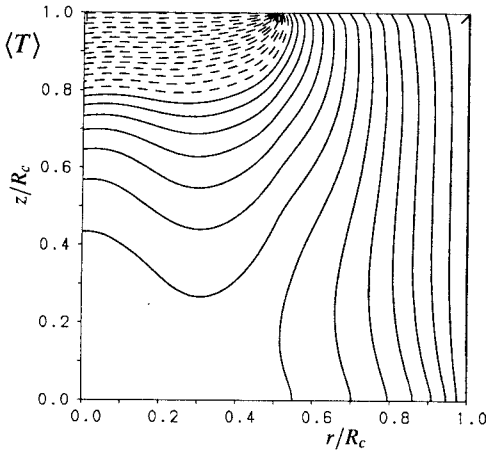


Figure 4: Mean isotherms of $DNS_1$ (reference case). Solid/dashed lines represent positive/negative values.

### Spatial resolution requirements

An upper limit for the mean mesh width $h_{min}$ of a DNS was derived by Grötzbach (Grötzbach 1983) demanding that the Kolmogorov length scale $l_k = (\varepsilon/\nu^3)^{1/4}$ has to be resolved on the mesh.

$$h = (r\Delta\varphi\Delta r\Delta z)^{1/3} \leq \pi(\nu^3/\varepsilon)^{1/4} \quad \text{or} \quad h_{min} = \pi/\varepsilon_{max}^{1/4} Gr^{-3/8} \tag{8}$$

In eq. (8) the dimensionless mean mesh width $h_{min}$ depends on the Grashof number and the dimensionless dissipation rate $\varepsilon$, which a

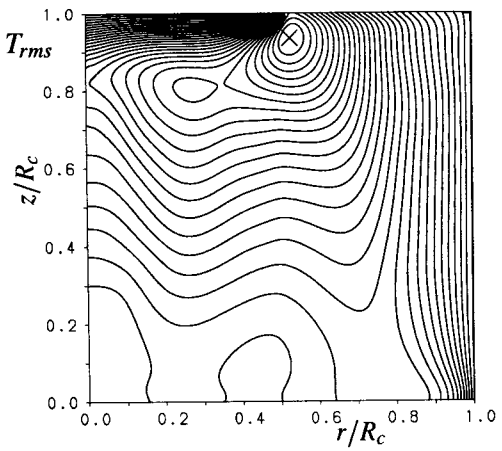


Figure 5: Contour lines of rms-temperature fluctuations of $DNS_1$ (reference case). $Max(x) : 0.17$.

priori is unknown. Evaluating $\varepsilon$ using $DNS_1$-data a maximum dissipation rate of $\varepsilon_{max} = 0.377$, which peaks just underneath the crystal edge and a volume averaged value $\bar{\varepsilon} = 0.0066$ was obtained. Subsituting $\varepsilon_{max}$ in eq. (8) leads to a mean mesh width $h_{min} = 0.0044$. This must be compared to the mean mesh width of $DNS_1$, which varies from $h = 0.00277$ at the centerline to $h = 0.0108$ at the crucible side wall. Taking into account that the dissipation rate peaks underneath the crystal edge for $r/R_c = 0.5$ and that $\varepsilon$ is considerably lower anywhere else in the flow, it is concluded that the grid is fine enough to resolve all the major physics.

**Numerical parameter study**

The streamlines of the mean velocities in Fig. 6 reflect the flow in the case of the smaller melt height ($DNS_2$), with the three major recirculation zones revealing similarities to the flow observed in $DNS_1$. As indicated by the dashed isotherms in Fig. 7 cold fluid extends over more than one half of the melt height. Although rotation rates of crucible and crystal are unchanged, the wetting surface at the crucible sidewall and consequently the influence of crucible rotation is reduced.

For the lower crystal rotation rate in $DNS_3$ streamlines of the mean velocity field and isotherms (not shown) reflect the same flow structure as presented in Fig. 6 for $DNS_2$. Even contours of rms temperature fluctuations of $DNS_2$ (lower melt height) and $DNS_3$ (smaller crystal rotation) and the position of their maximum values agree remarkably well. Therefore, for more information on the structure of rms temperature fluctuations in the case of $DNS_2$ and $DNS_3$ the reader is referred to Fig. 5 reflecting case $DNS_1$.

On the other hand lower crystal rotation rates and to some degree lower melt heights damp temperature fluctuations as indicated by the lower maximum $T_{rms}$ in Table 2. A strong change in the flow structure due to the high crystal rotation is visible in Fig. 8 ($DNS_4$). A single recirculation zone dominates the mean flow in the $(z,r)$-plane, while two smaller cells are observed close to the upper part of the crucible wall and below the free surface. Additionally, due to the increased rotation of the crystal, a small recirculation structure is created just underneath the crystal. Therefore mixing is enhanced within the crystallization zone leading to more uniform radial concentration gradients of impurities and dopants on the one hand. On the other hand this recirculation zone also acts as a trap for these substances. As indicated by the dashed isotherms in Fig. 9 cold fluid extends over more than one half of the melt height.

Table 2: Maxima of rms temperature fluctuations for $DNS_1$ - $DNS_8$

| DNS | 1 | 2 | 3 | 4 |
|---|---|---|---|---|
| $T_{rms,max}$ | 0.170 | 0.155 | 0.123 | 0.181 |
| DNS | 5 | 6 | 7 | 8 |
| $T_{rms,max}$ | 0.197 | 0.101 | 0.161 | 0.107 |

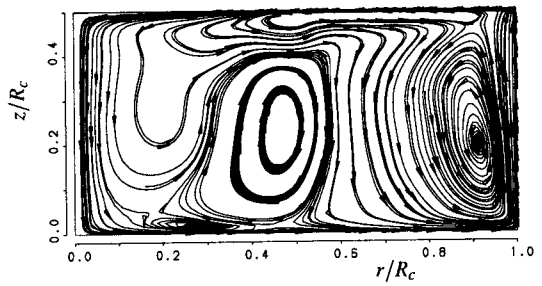


Figure 6: Streamlines of the mean velocity fields projected into $(z,r)$-planes of $DNS_2$ (low melt height).

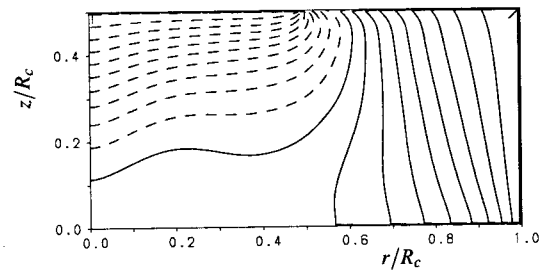


Figure 7: Mean isotherms obtained in $DNS_2$ (low melt height). Solid/dashed lines represent positive/negative values.

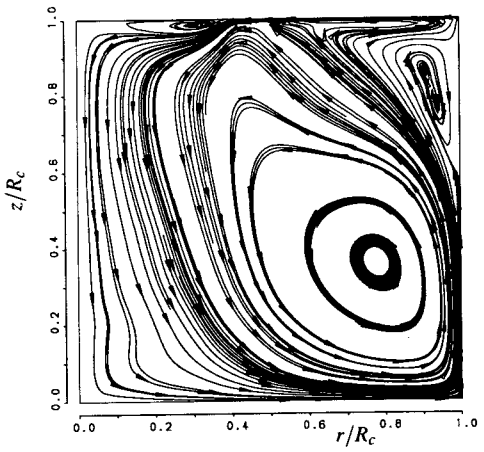


Figure 8: Streamlines of the mean velocity fields projected into $(z,r)$-planes of $DNS_3$ (high crystal rotation).

A shift towards the crucible bottom and axis of the position of maximum rms temperature fluctuation associated with an increased maximum value of $T_{rms} = 0.181(\approx 16.5K)$ is reflected in Fig. 10. Although temperature fluctuations of high amplitude are further increased for high crystal rotation rates, within the crystallization zone they are damped.

Increasing the Grashof number and the Marangoni number in $DNS_5$ does not significantly change the structure of the overall momentum and heat transport. Solely, the amplitude of maximum rms temperature fluctuations increases (see Table 2), but its position remains.

Finally in $DNS_6$ and $DNS_7$, heat radiation at the free surface is taken into account assuming a background temperature of $T_h = 1450K$. This has a remarkable effect on the radial heat flux close to the crystal edge as shown in Fig. 11. In contradiction to Fig. 5 the isotherms are almost uniformly distributed along the free surface, reflecting the decreased radial heat flux at the crystal edge. Obviously, this also reduces the spatial resolution requirements, which

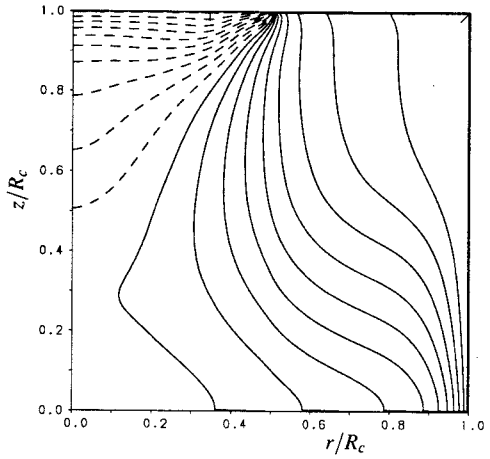


Figure 9: Mean isotherms of $DNS_3$ (high crystal rotation). Solid/dashed lines represent positive/negative values.

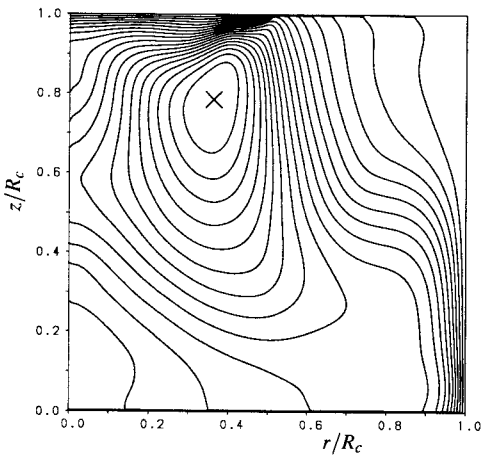


Figure 10: Isotherms of the rms fluctuating temperature of $DNS_4$ (high crystal rotation). $Max(\mathrm{x}) : 0.181$.

are extremly high close to the crystal edge due to high temperature and velocity gradients, if heat radiation is neglected. Besides modeling heat radiation at the free surface, the Marangoni number was reduced in $DNS_7$. The position of maximum rms temperature fluctuation which is shifted towards the cylinder axis, away from the crystal edge and the crystallization zone is shown in Fig. 13.

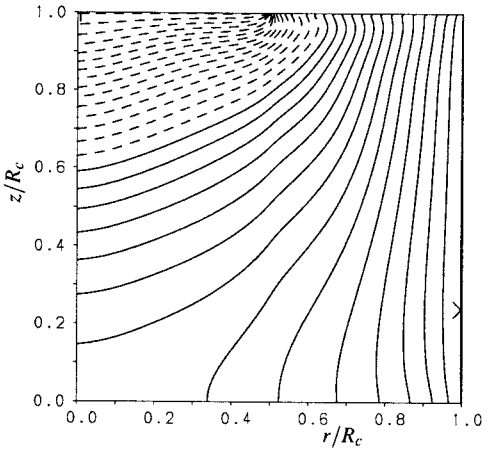


Figure 11: Isotherms of the rms fluctuating temperature of $DNS_6$ (heat radiation considered). Solid/dashed lines represent positive/negative values.

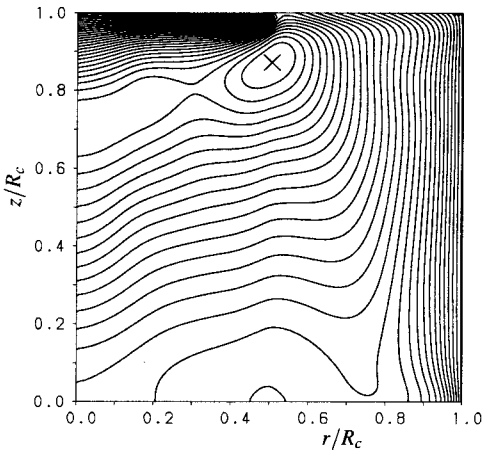


Figure 12: Isotherms of the rms fluctuating temperature of $DNS_6$ (heat radiation considered). $Max(\mathrm{x}) : 0.101$.

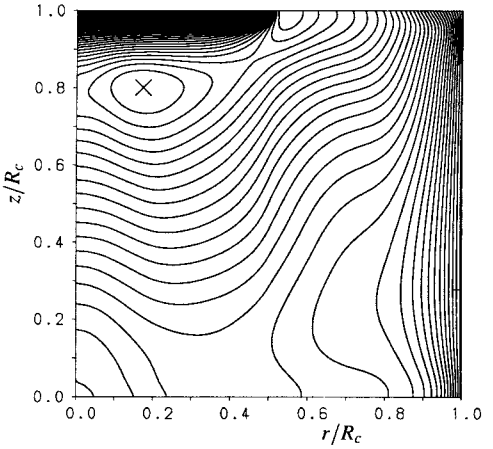


Figure 13: Isotherms of the rms fluctuating temperature of $DNS_7$ (small Marangoni number). $Max(\mathrm{x}) : 0.161$.

**Comparison to experiment**

$DNS_8$, the flow parameters of which are presented in Table 1, was conducted to compare computed temperature data to measurements, which were performed in a LEYBOLD EKZ 1300 crucible at Wacker Siltronic in Burghausen (Germany) (Wacker 2001). The same configuration was considered by Vizman et al. (Vizman 2001) and Enger et al. (Enger 2001). In order to ensure comparability of the computation with this experiment, the wall temperature distributions for the DNS were interpolated from measured temperatures according to:

$$T(z/R_c) = -4.6(z/R_c)^3 + 6.85(z/R_c)^2 - 3.615 z/R_c + 0.5, \quad (9)$$

$$T(r/R_c) = 0.619(r/R_c)^2 - 0.119. \quad (10)$$

Additionally heat radiation at the free surface was modelled using two different background temperature values, $T_h = 1510K$ for $5cm \leq r \leq 10cm$ and $T_h = 1560K$ between $r = 10cm$ and the wall.

The computed streamlines of the mean velocity fields are presented in Fig. 14. They indicate a flow, which is characterized by five major recirculation zones. The mean isotherms shown in Fig. 15 reveal a predominantly transversal orientation, for which the region of cold melt is increased. Contours of the rms temperature fluctuations demonstrate the existence of two characteristic regions of temperature fluctuations, one below the free surface with maximum values which are low compared to those in Table 2, and the other one below the crystal, where the contours are alligned with the crystal/melt interface.

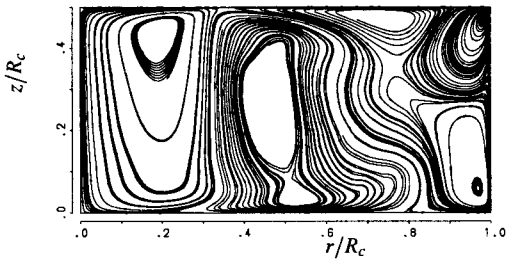


Figure 14: Streamlines of the mean velocity field of $DNS_8$.

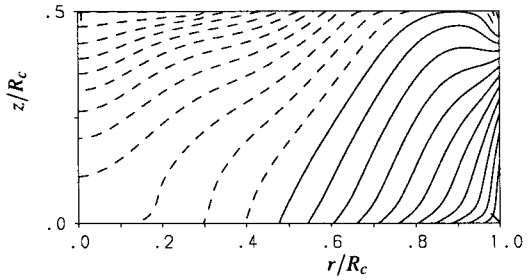


Figure 15: Isotherms of the mean temperature of $DNS_8$. Solid/dashed contour lines represent positive/negative values.

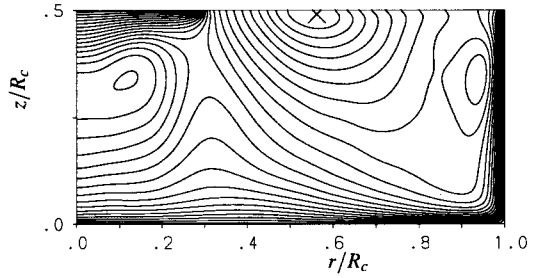


Figure 16: Contours of the rms fluctuating temperature of $DNS_8$. $Max(x) : 0.107$

The comparison of computed and measured values of mean temperature and rms temperature fluctuations for 9 different positions within the melt is presented in Table 3. The mean temperature values reveal differences of less than 6% of the overall mean temperature difference $\Delta T$. This underlines, that although the Czochralski process was idealized to some extent, the simulations produce reliable results. Somewhere higher differences for the rms temperature fluctuations are found. To understand this, it must be noted, that the thermocouples used for the measurements in the hot Si-melt do not capture high frequency temperature fluctuations. This might be the reason, why the measured rms temperature fluctuations are low compared to the simulation data for all locations depicted in Table 3.

Table 3: Comparison of measured and computed mean temperatures and rms temperature fluctuations

| $z/R_c, r/R_c$ | 0.44,0.24 | 0.32,0.24 | 0.21,0.24 |
|---|---|---|---|
| $\langle T \rangle_{num}$ | −0.33 | −0.19 | −0.13 |
| $\langle T \rangle_{exp}$ | −0.30 | −0.22 | −0.17 |
| $T_{rms,num}$ | 0.047 | 0.058 | 0.051 |
| $T_{rms,exp}$ | 0.037 | 0.045 | 0.0395 |
| $z/R_c, r/R_c$ | 0.44,0.43 | 0.32,0.43 | 0.21,0.43 |
| $\langle T \rangle_{num}$ | −0.248 | −0.121 | −0.059 |
| $\langle T \rangle_{exp}$ | −0.279 | −0.176 | −0.113 |
| $T_{rms,num}$ | 0.081 | 0.064 | 0.053 |
| $T_{rms,exp}$ | 0.034 | 0.047 | 0.042 |

## CONCLUSIONS

Direct Numerical Simulations of the turbulent flow in an idealized Czochralski crystal growth configuration have been performed for two melt heights, four different rotation rates of the crystal and crucible and for varying Marangoni and Grashof numbers.

While subjected to rotation by the crucible, the fluid is driven up the heated side wall by buoyancy and forced towards the crystal at the miniscus. From there surface tension drives the flow towards the crystal edge, where it encounters the centrifugally forced flow from underneath the crystal. The positions of maximum rms temperature and velocity fluctuations are located within the crystallization zone just underneath the crystal edge.

Decreasing either the melt height, the rotation rate of the crystal or changing the Grashof and/or Marangoni number leads to minor changes in the bulk flow structure. Especially for low melt heights an increased influence of cold fluid increases the possibility of undercooling of the melt underneath the crystal, while rms temperature fluctuations decrease slightly.

Strong changes in the bulk flow structure are observed for high rotation rates of the crystal. The increased centrifugal forces underneath the crystal drive one major recirculation zone. Maximum rms temperature fluctuations increase with the rotation rate of the crystal. The position of maximum values moves towards the crucible bottom for $DNS_4$ (high crystal rotation rate). This shifted position of maximum rms temperature fluctuations, which is also observed if heat radiation is modelled and the Marangoni number is decreased might lead to more friendly crystal growth conditions. The trade-off probably is a reduced mixing underneath the crystal, where impurities and dopant might be trapped in a small recirculation zone.

Good agreement of mean temperatures, which differed by less than 6%, was obtained in a comparison of computed and measured temperatures. This underlines that idealization of the industrial Czochralski process is justified.

## REFERENCES

Enger, S., Gräbner, O., Müller, G., Breuer and M., Durst, F., 2001, "Comparison of measurements and numerical simulations of convection on Czochralski crystal growth of silocon", *Journal of Crystal Growth*, Vol. 230, p. 135-142.

Grötzbach, G., 1983, "Spatial resolution requirements for direct numerical simulation of the Rayleigh-Bénard convection", *Journal of Comp. Phys.*, Vol. 49, pp. 241-264.

Jones, A.D.W, 1989,"Flow in a Model Czochralski Oxide Melt.", *Journal of Crystal Growth*, Vol. 94, pp. 421-432.

Kuroda, E., Kozuka, H. and Takana, Y., 1982, "Influence of Growth Conditions on Melt Interface Temperature Oscillations in Silicon Czochralski Growth", *Journal of Crystal Growth*, Vol. 68, p. 613.

Schumann, U., 1973, "Ein Verfahren zur direkten numerischen Simulation turbulenter Strömungen in Platten- und Ringspaltkanälen und über seine Anwendung zur Untersuchung von Turbulenzmodellen", Dissertation, University of Karlsruhe.

Vizman, D., Gräbner, O. and Müller, G., 2001, "Three-dimensional numerical simulation of thermal convection in an industrial Czochralski melt: comparison to experimental results", *Journal of Crystal Growth*, Vol. 233, p. 687-698.

Wacker Siltronic GmbH, 2001, private communication.

Wilcox, W.R. and Fullmer, L.D., 1965, "Turbulent free convection in Czochraski crystal growth ", *Journal of Appl. Phys.*, Vol. 36, No. 7, pp. 2201-2206.